

Work-Function-Tunable MXenes Electrodes to Optimize p-CsCu₂I₃/n-Ca₂Nb_{3-x}Ta_xO₁₀ Junction Photodetectors for Image Sensing and Logic Electronics

Jiaxin Chen, Xinya Liu, Ziqing Li, Fa Cao, Xiang Lu, and Xiaosheng Fang*

Tunable work function has a high profile for the MXene-based optoelectronic devices, and surface modification provides the huge potential to shift its Fermi level and modulate the work function. In this work, the window of MXene's work function is engineered from 4.55 to 5.25 eV by surface modification with LiF, Se, and polyethylenimine ethoxylated (PEIE). The vertical p-CsCu₂I₃/n-Ca₂Nb_{3-x}Ta_xO₁₀ junction photodetectors are constructed on the basis of the above surface-modified MXenes, which changes the Schottky barrier between n-Ca₂Nb_{3-x}Ta_xO₁₀ and the electrodes. In particular, the rectification effect is significantly enhanced by utilizing PEIE-decorated MXene electrodes, resulting in a high rectification ratio of 16 136 and improved UV responsivity of 81.3 A W⁻¹. Such high-performance devices based on MXenes electrodes are compatible with the standard clean room fabrication process, realizing large-scale flexible UV detectors that maintain 80% of the original current after 5000 times bending. Meanwhile, a photodetector array stimulated with UV of different wavelengths is constructed to reveal its potential for image sensing. Finally, functional "AND" and "OR" optoelectronic logic gates are developed for UV communication using Au/CsCu₂I₃/Ca₂Nb_{3-x}Ta_xO₁₀/MXene-PEIE photodetectors, enriching the application of MXene-based optoelectronic devices. This work on tuning MXene work function via surface modification demonstrates that MXene is a promising candidate for future optoelectronics.

1. Introduction

Electrode work function is a very important parameter to determine the junction at the contact between metallic electrodes and semiconductor materials, which is the heart of modern optoelectronics.^[1] To realize high-performance photodetectors, the carefully designed device structure and tailored energy band alignment are required to enhance highly efficient carrier collection at the selective electrodes. Photodetectors based on p-n junctions are often endowed with high responsivity and sensitivity due to the low dark currents, and usually, the electrode


film with high work function is chosen to collect holes, and the one with a lower work function will be set on the other side of the junction to collect electrons for tuning the energy level alignment.^[2]

Recently, 2D materials have emerged as an insertion layer to reduce the defects at the interface and engineer the energy alignment to improve the charge injection and extraction process, and they finally enhance the charge collection efficiency at the electrodes. MXenes are a series of 2D metal carbides and nitrides and most of them are metallic conductors.^[3] They are usually provided with intrinsically high electronic conductivity, moreover, the abundant surface terminations offer the possibility to alter the Fermi level, giving them electronically tunable work function.^[4-6] In the field of photodetection, MXenes can be applied as photore sponsive materials,^[7,8] yet mostly MXenes are well developed when being used as the electrode materials of optoelectrical devices for high conductivity and transmittance,^[9,10] and the barrier between semiconductors and electrodes can be

tuned according to the work function of MXenes for different purposes.^[11,12] The Schottky barrier between MXene and semiconductors could inhibit the backflow of electrons and improve the charge separation^[13,14] to realize high-performance self-powered photodetectors.^[15] Meanwhile, it is also reported that the work function of some MXenes matches well with oxide thin-film transistors, such as ZnO and SnO, forming good Ohmic contact interface.^[16]

It is proved that the surface electrostatic potential of MXenes is usually decided by functional groups during the etching process, and the work function can be tuned in a wide range from 1.6 to 6.2 eV,^[17] which could be used to modify the work function and the band alignment of electronic devices.^[18,19] It is also confirmed that the different surface terminations realized through altering annealing temperatures could significantly affect the work function upon heating in vacuum.^[20] And the nonlinear relationship exists between the work function and the relative concentrations of OH, O, and F terminations.^[21] Although the work function of MXenes can be changed via adjusting the ratio of OH, O, and F terminations, the process is complex to handle and the resulting work function is difficult to

J. Chen, X. Liu, Z. Li, F. Cao, X. Lu, X. S. Fang
Department of Materials Science
Fudan University
Shanghai 200438, China
E-mail: xshfang@fudan.edu.cn

 The ORCID identification number(s) for the author(s) of this article can be found under <https://doi.org/10.1002/adfm.202201066>.

DOI: 10.1002/adfm.202201066

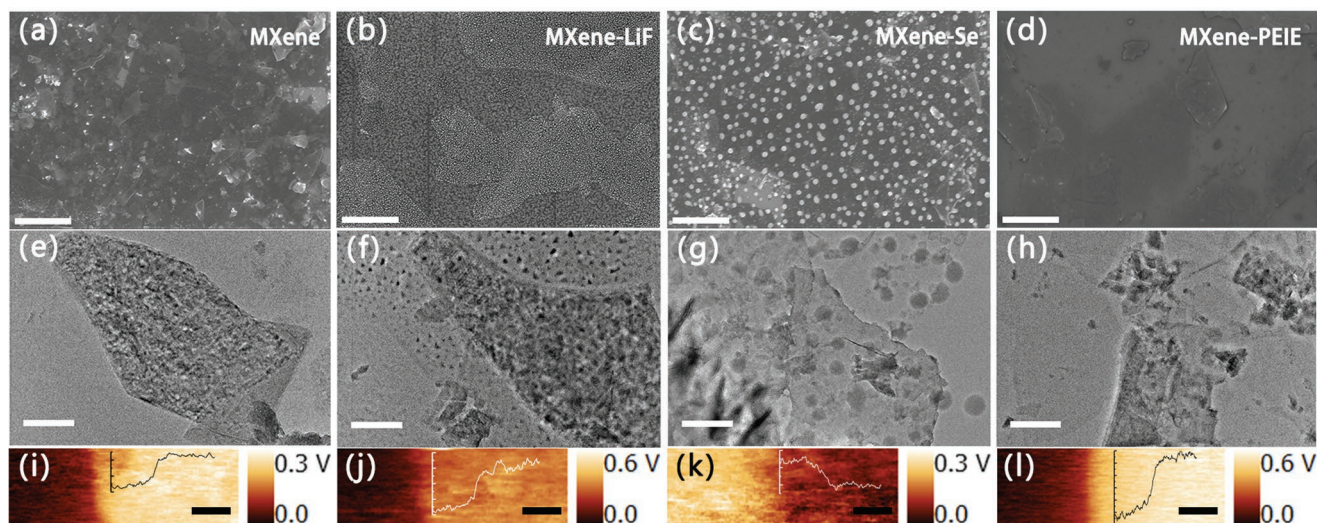


Figure 1. SEM images of a) pristine MXene film, b) MXene–LiF film, c) MXene–Se film and d) MXene–PEIE film, scale bar: 1 μm . TEM images of e) pristine MXene flakes, f) MXene–LiF flakes, g) MXene–Se flakes, and h) MXene–PEIE flakes, scale bar: 200 nm. KPFM results of i) pristine MXene film, j) MXene–LiF film, k) MXene–Se film and l) MXene–PEIE film, scale bar: 1 μm .

be precisely controlled. There is also research of MXene surface functionalization for engineering the window of its work function.^[22] Jing et al. used diazonium covalent modulation and regulated its quantity, gaining an adjustable work function range of 0.58 eV, but $\text{Ti}_3\text{C}_2\text{T}_x$ conductivity was also reduced due to the electron-withdrawing effect of surface functionalization.^[23] Lyu et al. applied chemical doping with NH_3 to reduce the work function of MXene and formed Ohmic contact with n-type organic field-effect transistors (OFETs).^[24] Guo et al. applied Fe terminations on $\text{Ti}_3\text{C}_2\text{T}_x$ for a lower work function to efficiently transfer electrons.^[25] Wang et al. modulated the work function of a 0.47 eV decrease by blending didecylmethyl ammonium bromide (DDAB) with $\text{Ti}_3\text{C}_2\text{T}_x$ which also enhanced the electron mobility.^[26] In brief, the surface-modified MXenes used for photodetectors require high transmittance, high conductivity, and a wide range of tunable work function to improve the contact condition.

Herein, the surface of $\text{Ti}_3\text{C}_2\text{T}_x$ is modulated through LiF, Se, and PEIE functionalization, realizing a window of work function from 4.55 to 5.25 eV. In our work, these strategies provide methods for both positive and negative changes in MXene's work function. There are reports about significantly affecting work function by LiF and PEIE decoration, for example, the work function of ITO could be affected by LiF particles,^[27] and the PEIE deposition would lower the work function.^[28,29] However, such modification has not been applied to MXene-based electrodes yet and its effects remains unknown. On the basis of Kelvin probe force microscopy (KPFM) results, the influence of surface decoration with LiF, Se and PEIE on MXenes work function was revealed, and the p-CsCu₂I₃/n-Ca₂Nb_{3-x}Ta_xO₁₀ inorganic perovskite junction was constructed using different kinds of MXenes as electrodes. When the work function was reduced via LiF and PEIE modulation, the rectification ratio of the p–n junction was significantly enhanced, especially with MXene–PEIE electrodes the ratio rising 94-fold in contrast to pristine MXene electrode. Meanwhile, the way of increasing its work function was also put forward by Se decoration and

the rectification effect of p–n junction could be suppressed. Moreover, the device was fabricated through standard clean-room processes of photolithography that could be applied for large-scale flexible optoelectronic arrays, and the device on polyethylene terephthalate (PET) substrate could survive 5000 times folding. Additionally, MXene electrodes could be used for large-scale image sensor arrays^[30,31] Here, an 8×8 array was designed to demonstrate the image sensing potential by using UV of different wavelengths. At last, the logic gates of “AND” and “OR” were designed using the Au/CsCu₂I₃/Ca₂Nb_{3-x}Ta_xO₁₀/MXene–PEIE devices to exhibit its huge potential for optoelectronic circuits and optical communications. This work highlights an approach to tune the work function of MXenes in a wide range and proposes new ideas for their potential applications in the optoelectronics field.

2. Results and Discussion

At first, scanning electron microscope (SEM) was performed to gain the sight of MXenes morphology after surface modification. **Figure 1a–d** is the SEM details of the surface-modified MXenes, which are: pristine MXene, MXene with thermal evaporated LiF nanoparticles (named by MXene–LiF, the same below), MXene with thermal evaporated Se particles (MXene–Se) and MXene covered by PEIE layer (MXene–PEIE). Compared with the smooth surface of $\text{Ti}_3\text{C}_2\text{T}_x$ nanoflakes in **Figure 1a**, LiF and Se nanoparticles can be clearly seen attaching on the surface of few-layered MXene flakes in **Figure 1b,c**, respectively. LiF particles are about 20 nm in size, while Se particles are about 50 nm, and both of them are uniformly distributed on the $\text{Ti}_3\text{C}_2\text{T}_x$ flakes. With PEIE covering, the MXene flakes present a cleaner surface as shown in **Figure 1d**. The atomic force microscope (AFM) images of above surface-modified MXenes films are shown in **Figure S1** (Supporting Information), indicating the smooth and continuous surface of MXenes films for electrodes. Transmission electron microscope

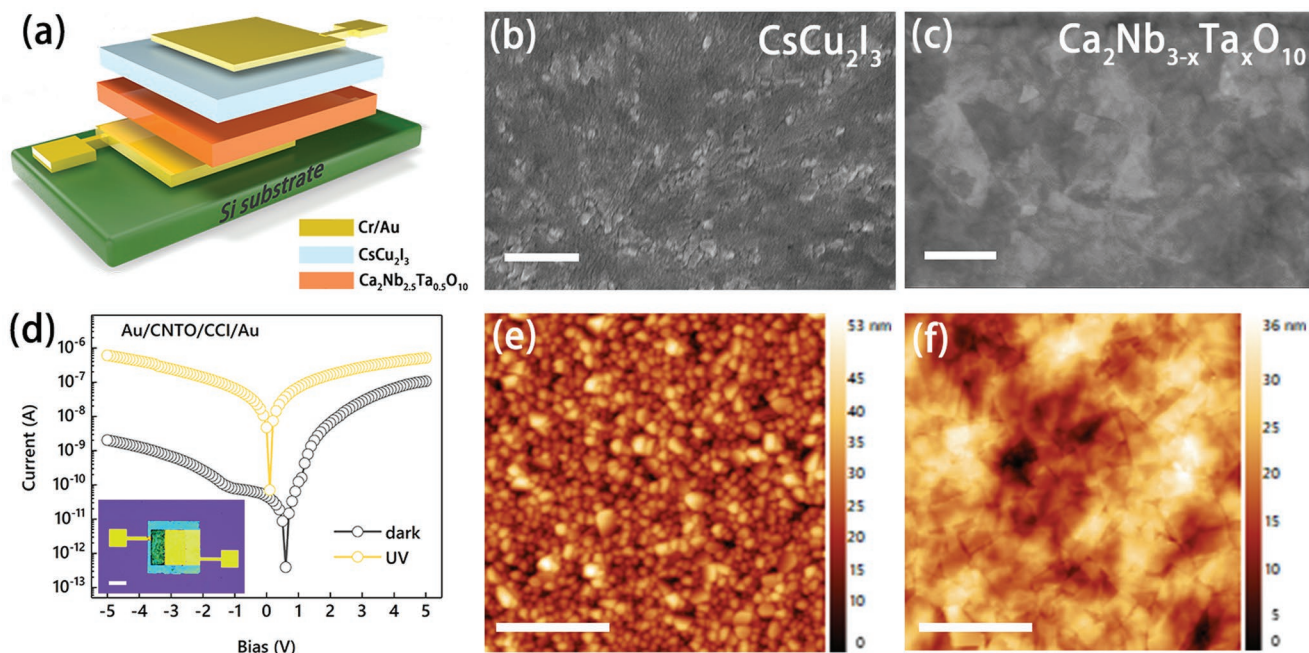


Figure 2. a) Scheme of Au/p-CsCu₂I₃/n-Ca₂Nb_{3-x}Ta_xO₁₀/Au device. SEM image of b) thermal evaporated CsCu₂I₃ films and spin-coated Ca₂Nb_{3-x}Ta_xO₁₀ film, scale bar: 1 μm. d) *I*-*V* curves of photoresponse of Au/p-CsCu₂I₃/n-Ca₂Nb_{3-x}Ta_xO₁₀/Au device. The inset is the optical micrograph of Au/p-CsCu₂I₃/n-Ca₂Nb_{3-x}Ta_xO₁₀/Au device, scale bar: 100 μm. e) AFM image of CsCu₂I₃ films on Ca₂Nb_{3-x}Ta_xO₁₀ films and f) AFM image of Ca₂Nb_{3-x}Ta_xO₁₀ films on Si substrate, scale bar: 1 μm.

(TEM) images of above MXenes in Figure 1e–h further clarify the size and uniform distribution of surface modifications on few-layered MXene flakes. High-resolution transmission electron microscope (HRTEM) and selected area electron diffraction (SAED) images in Figure S2 (Supporting Information) further proved the crystal quality of MXenes nanoflake films. The X-ray diffraction (XRD) patterns of four kinds of MXenes films are summarized in Figure S3 (Supporting Information) to analyze the formation and crystalline nature of the MXene, appearance of almost only one intense (002) peak indicating successful etching of Ti₃AlC₂. Moreover, Kelvin probe force microscope (KPFM) tests were performed to explore the change of surface potential after surface modification. Before the test, each sample was evaporated with 30 nm Au film for work function calibration. Figure 1i–l all show a clear step between Au (the left part of each sample) and MXenes. With Au calibration (whose work function is agreed to be 5.1 eV), it is validated that the work function of MXene is 4.9 eV, since its surface potential increases by about 0.2 V compared with Au. MXene–Se has a higher work function of 5.25 eV, while MXenes–LiF and MXene–PEIE have lower values of 4.85 eV and 4.55 eV, respectively. The Raman spectra of four MXenes are shown in Figure S4 (Supporting Information). Except from the resonant peak, the E_g vibration modes correspond to in-plane vibration and the A_{1g} modes demonstrate out-of-plane vibration of Ti and C atoms.^[32,33] To check the influence of surface modification on MXene’s optical and electrical performance, the transmittance of four MXenes of the same sheet resistance of about 2 kΩ was revealed in Figure S5 (Supporting Information). And it is proved that the electrical conductivity has not been affected by surface modification, and all the MXene films have high trans-

mittance of nearly 90%. The strong absorption in UV range results from interband transitions of MXene.^[5] The X-ray photoelectron spectra (XPS) in Figure S6 (Supporting Information) also demonstrate the surface chemistry change after surface modification. From the survey spectra of four MXenes, when MXene is decorated with LiF particles, the F 1s signal is significantly enhanced. And when MXene is loaded with Se or organic PEIE, the Se 3d peaks and N 1s peaks are detected, respectively. The high-resolution XPS spectra has more detailed description of surface chemistry, which demonstrates the presence of terminal groups and surface decorations. For instance, when MXene is combined with PEIE the F 1s peaks have a lower binding energy for obtaining electrons as shown in Figure S6 (Supporting Information), demonstrating the effect of surface modification.^[18]

To reveal the application of tunable work function of these four MXenes, we constructed a p–n junction photodetector using n-typed perovskite Ca₂Nb_{3-x}Ta_xO₁₀ and p-typed perovskite CsCu₂I₃. They have a wide bandgap of 3.34 and 3.51 eV respectively, which is calculated according to the absorption spectra in Figure S7 (Supporting Information). CsCu₂I₃ film responds to UV–vis light with fast speed, which is synthesized through thermal evaporation.^[30,34] Ca₂Nb_{3-x}Ta_xO₁₀ is a kind of B-site substituted 2D layered calcium niobates by Ta which has a high responsivity towards UV light.^[35] The neat and clean surface of p-CsCu₂I₃ and layered structure of n-Ca₂Nb_{3-x}Ta_xO₁₀ are shown in Figure 2b,c. XRD patterns of the two wide-bandgap materials are displayed in Figure S8 (Supporting Information). The p-type perovskite CsCu₂I₃ has a polycrystalline structure and high purity for the pattern fits well with the PDF#45-0076.^[36,37] Compared with the patterns of HCa₂Nb₃O₁₀ (PDF#40-0884),^[38]

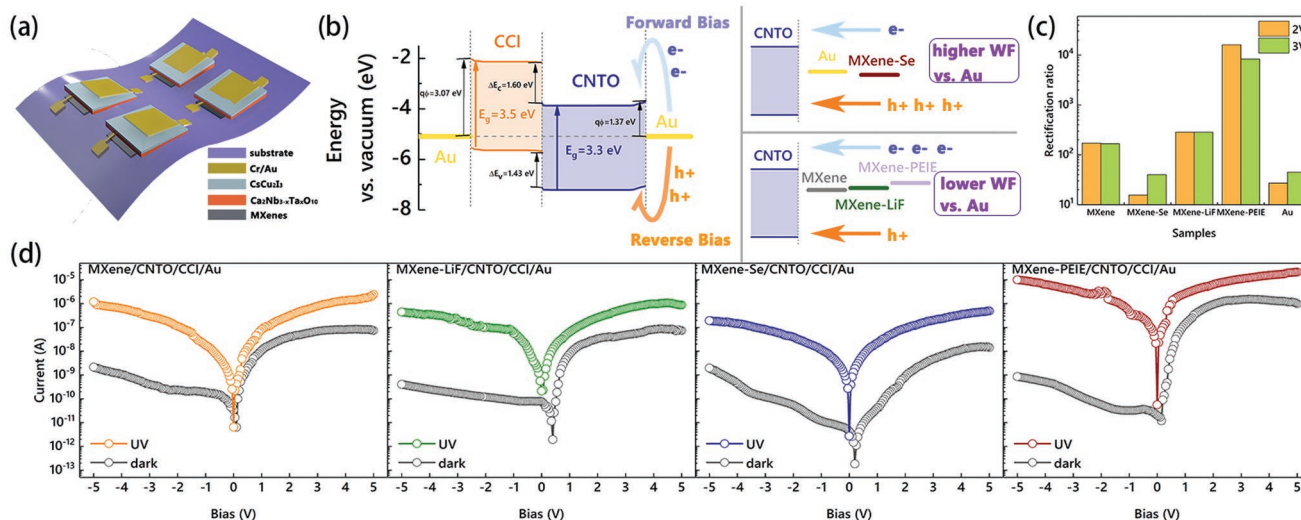


Figure 3. a) Scheme of Au/p-CsCu₂I₃/n-Ca₂Nb_{3-x}Ta_xO₁₀/MXenes device with different MXenes as bottom electrodes. b) Energy band diagram of Au/p-CsCu₂I₃/n-Ca₂Nb_{3-x}Ta_xO₁₀/MXenes device. WF: work function. c) Rectification ratio of photodetectors using different electrodes. d) *I*-*V* curves of photoresponse under UV illumination of Au/p-CsCu₂I₃/n-Ca₂Nb_{3-x}Ta_xO₁₀/MXene, Au/p-CsCu₂I₃/n-Ca₂Nb_{3-x}Ta_xO₁₀/MXene–Se, Au/p-CsCu₂I₃/n-Ca₂Nb_{3-x}Ta_xO₁₀/MXene–LiF and Au/p-CsCu₂I₃/n-Ca₂Nb_{3-x}Ta_xO₁₀/MXene–PEIE.

Ca₂Nb_{3-x}Ta_xO₁₀ also has high purity without a second phase. The high-resolution XPS spectra of CsCu₂I₃ and Ca₂Nb_{3-x}Ta_xO₁₀ are shown in Figure S9 (Supporting Information) to further describe their chemistry states. Their valence band positions are also confirmed to verify their types and show the device's band alignment. Figure 2a shows the structure of the device, where CsCu₂I₃ layer and Ca₂Nb_{3-x}Ta_xO₁₀ layer are in a vertical stack and they are sandwiched between Au bottom electrode and Au top electrode. The inset of Figure 2d is the optical micrograph of the p–n junction device. To ensure there is no Schottky barrier resulting from asymmetric electrode areas, the bottom electrode and the top electrode are designed to the same figure and size. The surface roughness of the two semiconductor layers is also shown in Figure 2e,f. The average roughness of CsCu₂I₃ (named by CCI) layer on Ca₂Nb_{3-x}Ta_xO₁₀ layer and Ca₂Nb_{3-x}Ta_xO₁₀ (named by CNTO) layer on Si substrates are 5.28 and 4.31 nm, respectively, demonstrating the high smoothness of the layer-by-layer structure. Their work functions are also determined through KPFM measurements in the same way as MXenes as shown in Figure S10 (Supporting Information). The device reveals an obvious photoresponse under UV stimulation as shown in Figure 2d and the on/off ratio reaches nearly 10³ at a reverse bias of –5 V.

Further, the Au bottom electrode can be replaced by four kinds of MXene electrodes as shown in Figure 3a. In Figure 3d, the photoresponse current–bias (*I*-*V*) curves are listed to show the influence of MXene's tunable work function. It could be seen that the photocurrent values of each device are almost the same, except that the photocurrents of MXene–PEIE device are slightly higher. When Au bottom electrode was replaced by pristine MXene, the rectification ratio of the device under the dark was apparently boosted. And when the work function was decreased by utilizing MXene–LiF and MXene–PEIE bottom electrodes, the rectification was further improved. Especially, the rectification ratio of MXene–PEIE diode reaches as high as 16 136 at ±2 V bias, which is 94 times higher than that of

MXene/CNTO/CCI/Au diode and 664 times higher than that of Au/CNTO/CCI/Au diode. However, when Au bottom electrode was replaced by MXene–Se, the rectification was suppressed by comparison with Au or MXene bottom electrodes, as shown in Figure 3c. To figure out the reason of rectification ratio changes, the energy band diagram in thermal equilibrium state of all the device is listed in Figure 3b. The positions of conduction band and valence band of p–n junction are set according to KPFM results in Figure S10 (Supporting Information), and the electron affinity of CNTO is 3.73 eV. On the p-type CsCu₂I₃ side, Au is used to form an ohmic contact, which is further confirmed by Figure S11 (Supporting Information) where the resulted current and the applied bias of Au/CCI/Au device has a linear relationship. When both bottom and top electrodes of p–n junction are Au (work function = 5.1 eV), there will be a Schottky barrier (1.37 eV) between n-type CNTO layer and Au bottom electrode. When using electrodes with lower work function on the CNTO side, such as MXene (work function = 4.9 eV), the Schottky barrier (1.17 eV) is supposed to be reduced. Thus, when the forward bias is applied across the whole p–n junction, the electron current from MXene to CNTO will be enlarged. On the contrary, the hole current will be suppressed when reverse bias is applied. This process will improve the dark current at forward bias, and lower the current at reverse bias, which boosts the rectification ratio and increases the on/off ratio of photocurrent at the reverse bias. When using electrodes with lower work function, MXene–LiF (work function = 4.85 eV) and MXene–PEIE (work function = 4.55 eV), the effect of lowering dark current under reverse bias will be more significant. However, if the Au electrode on the n-type CNTO side is replaced by high-work-function MXene–Se (work function = 5.25 eV) film, the Schottky barrier (1.52 eV) between CNTO and the electrode will be further enlarged. And consequently, at reverse bias, the on/off ratio will be reduced and the rectification ratio will also fall.

On the basis of above discussion, we finally chose MXene–PEIE with low work function of 4.55 eV as the bottom electrode

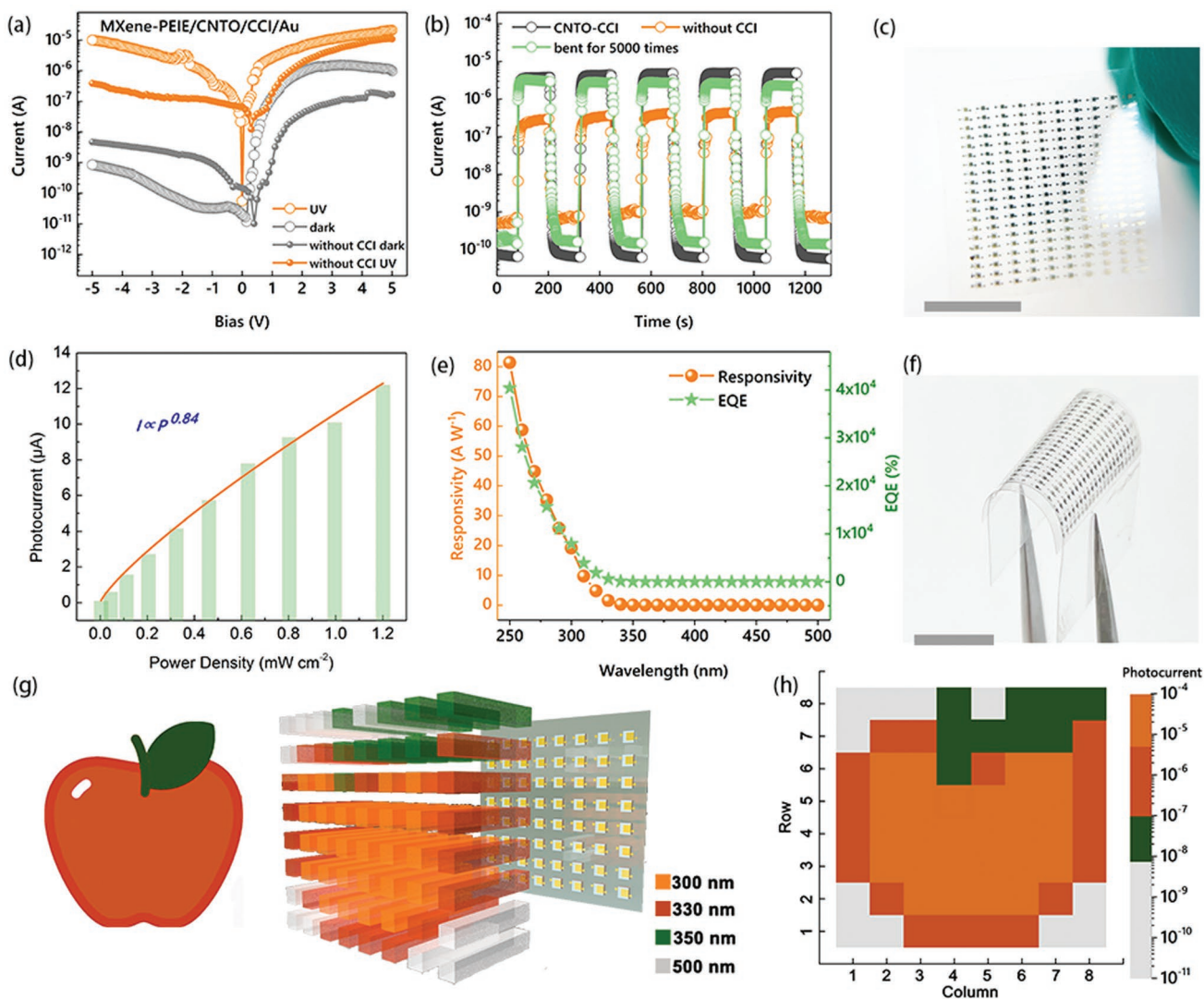


Figure 4. a) I - V curves of Au/p-CsCu₂l₃/n-Ca₂Nb_{3-x}Ta_xO₁₀/MXene-PEIE device and Au/p-CsCu₂l₃/MXene-PEIE device under dark condition and UV illumination. b) I - t curves under bias of -3 V of Au/p-CsCu₂l₃/n-Ca₂Nb_{3-x}Ta_xO₁₀/MXene-PEIE device on Si substrate (dark gray), Au/p-CsCu₂l₃/MXene-PEIE device (orange), and Au/p-CsCu₂l₃/n-Ca₂Nb_{3-x}Ta_xO₁₀/MXene-PEIE on PET substrate after 5000 times bending (green). c) Photograph of Au/p-CsCu₂l₃/n-Ca₂Nb_{3-x}Ta_xO₁₀/MXene-PEIE on PET substrate. Scale bar: 5 mm. d) The relationship between photocurrent and UV power density under bias of -5 V. e) The responsivity and EQE of Au/p-CsCu₂l₃/n-Ca₂Nb_{3-x}Ta_xO₁₀/MXene-PEIE under illumination of various wavelength under bias of -5 V. f) Photograph of Au/p-CsCu₂l₃/n-Ca₂Nb_{3-x}Ta_xO₁₀/MXene-PEIE on PET substrate being bent at the degree of 180°. Scale bar: 5 mm. g) Schematic image of UV sensing array. h) Photocurrents mapping results of 8 × 8 UV image sensing array.

to reduce the Schottky barrier, and the control sample of MXene-PEIE/CNTO/Au was also set to explain the influence of adding p-type CCI layer. As seen from **Figure 4a**, there is a rise in the dark current and the photocurrent decreases without CCI layer. This is also confirmed by current-time (I - t) curves in **Figure 4b**. Judging from above, the p-type layer increases the on/off ratio by constructing a built-in electric field which helps to suppress the carrier transport under dark condition and promote the photo-induced carriers separation. The I - t curves also verified the stability of photoresponse, and the response speed of this device is about several seconds (rise time 12.9 s/fall time 1.82 s). To present the device in a form suitable for large-scale production and flexible electronics, the device was constructed as arrays via standard clean room process on an ultraflexible PET film. The

digital photo of this flexible array is shown as **Figure 4c**. After being bent at an angle of 180° as **Figure 4f** shown for 5000 times, the photocurrent is still very stable and keeps 80% of the original current. The relationship between photocurrent and UV power density is also explored as shown in **Figure 4d** and it is fitted as

$$I \propto P^{0.84} \quad (1)$$

where I represents photocurrent and P represents UV power density. The responsivity and external quantum efficiency (EQE) of this device is calculated as^[39-41]

$$R_{\lambda} = \frac{I_{\text{photo}} - I_{\text{dark}}}{PS} \quad (2)$$

$$EQE = \frac{hc}{q\lambda} R_{\lambda} \quad (3)$$

where I_{photo} and I_{dark} refer to photocurrent and dark current, S represents the area of p-n junction layer, and R_{λ} refers to the responsivity under UV stimulation of different wavelength λ . With the decreasing wavelength, the responsivity increases and reaches the highest value of 81.3 A W^{-1} under 250 nm illumination, at the meantime the EQE reaches as high as $4.04 \times 10^4\%$. The MXene-based photodetector could be utilized to perform spatial and colorimetric measurements. An image sensor made of an 8×8 array of UV photodetectors was constructed and Figure 4g showed a schematic image of UV sensing array. Stimulation irradiation was set with four kinds of monochromatic light whose wavelengths were 300, 330, 350, and 500 nm. The figure of an apple picture was outlined by different stimulation irradiation which would excite corresponding photocurrents of different orders of magnitude at each photodetector pixel. The resulting photocurrents at each pixel were listed in Table S1

(Supporting Information), and the original current mapping was shown in Figure S12 (Supporting Information). When resulting photocurrents under -5 V bias were collected, by changing the scale bar color, the current mapping results would reflect the stimulated image as exhibited in Figure 4h. This MXene-based image sensor array ensures fair use of responsivity curves (Figure 4e) and paves a versatile way for future UV image sensors.

Optoelectronic logic gates are attracting much attention for combining optical and electrical signals together to increase the integration density and create versatile functionality of optoelectronic integrated circuits.^[42–44] The optoelectronic logics are further designed as Figure 5c to exhibit the potential of this photodiode. Figure 5a,b are the optical micrographs of the AND and OR logic gates formed from two photodiodes. For the AND gate, two diodes in series connection are marked as Input A and Input B, respectively. And for the OR gate the two diodes are in parallel connection and also marked as shown in Figure 5b. The input signal is denoted with “1” when UV light is shed on one

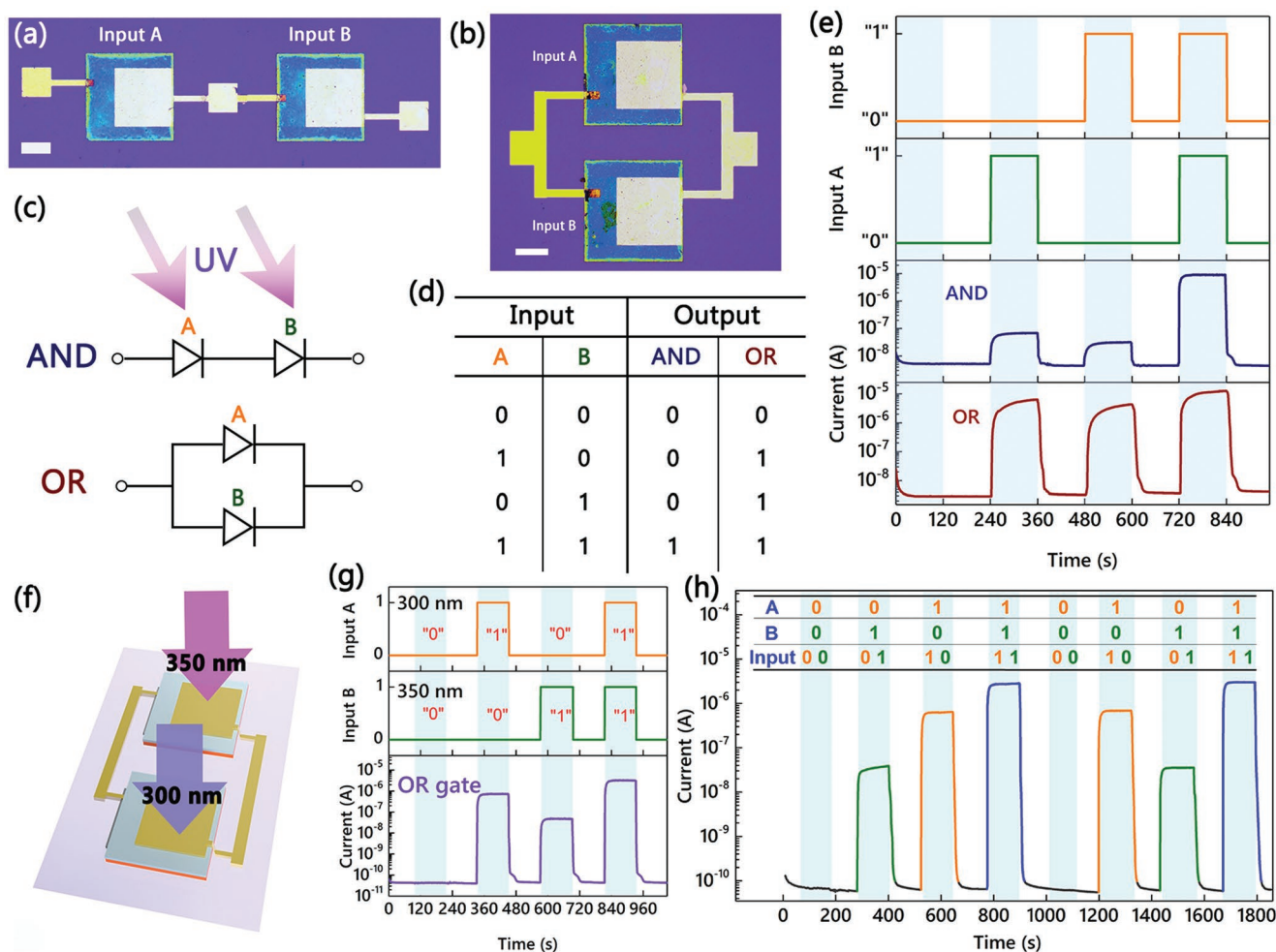


Figure 5. a) The optical micrograph of AND gate by combining two Au/CsCu₂I₃/Ca₂Nb_{3-x}Ta_xO₁₀/MXene-PEIE device in series connection, scale bar: 100 μm . b) The optical micrograph of OR gate by combining two Au/CsCu₂I₃/Ca₂Nb_{3-x}Ta_xO₁₀/MXene-PEIE device in parallel connection, scale bar: 100 μm . c) The circuits scheme of AND and OR gates. d) The truth table of AND and OR gates. e) The $I-t$ curves of AND and OR optical logic gates. f) Scheme of OR gate irradiated with 300 and 350 nm. g) The $I-t$ curves of OR gate stimulated with dual wavelengths. h) Resulting two-byte signal of “00011011” and “00100111.”

diode, and referred as “0” without UV stimulation. The input signal is set as Figure 5e with 120 s duration and an interval of 120 s. The resulting photocurrent is also shown in Figure 5e. If we consider the output currents under 10^{-6} A (which is set as beyond detection) as the “0” and above ones as “1,” the truth table can be acquired as Figure 5d. The minor photocurrents of AND circuits during 240–720 s are resulting from the influence of scattered light to the other device. To show the potential of the photodetector logic circuits for future UV communication, dual-wavelength irradiation was adopted as Figure 5f showed. When “Input A” of OR gate was stimulated by 300 nm and “Input B” was irradiated with 350 nm, the resulting photocurrents of different orders of magnitude could be considered as different signals (Figure 5g). The photocurrent of about 3×10^{-6} A reflected input signal of “1” “1,” while nearly about 1×10^{-6} A was “1” “0” and 3×10^{-8} A demonstrated “0” “1.” During the test period, combining diverse input signals would form corresponding photocurrents arrangements, which could be utilized for UV communication. For instance, Figure 5h described a two-byte signal “00011011” and “00100111.” The results provide a practical solution for future applications in UV optical communication.

3. Conclusion

In summary, we have successfully tuned the work function of MXenes for both positive and negative changes by different methods of surface modification, realizing a work function window of 4.55–5.25 eV. The PEIE-modified MXene film owned a work function of 4.55 eV and it was applied to p-CsCu₂I₃/n-Ca₂Nb_{3-x}Ta_xO₁₀ vertical junction photodetector as the bottom electrode. The Au/CsCu₂I₃/Ca₂Nb_{3-x}Ta_xO₁₀/MXene-PEIE device reached a high rectification ratio of 16 136, which was much higher than using Au or pristine MXene electrodes. The enhanced rectification effect was originated from the reduced Schottky barrier due to low work function of MXene-PEIE. The optimized photodetector also could be integrated on ultra-flexible PET substrates for being utilized as large-scale flexible optoelectronic devices and it could survive 5000 times bending with 80% of original photocurrent kept. The application of Au/CsCu₂I₃/Ca₂Nb_{3-x}Ta_xO₁₀/MXene-PEIE device was further broadened by constructing an 8 × 8 array of UV photodetectors. Irradiated with UV lights of four different wavelength, the UV sensing array could reflect the target image by demultiplexing the desired photocurrents. What's more, by combining two devices AND and OR optoelectronic logic gates were designed for UV photocommunications. It is believed that this work provides new methods for tuning the work function of MXenes and broadens application of MXenes to the modern optoelectronic interconnected circuits.

4. Experimental Section

Synthesis of MXene Nanoflakes: The synthesis process is according to the literature.^[45] 1g LiF was added into 20 mL 9 M HCl and the solution was stirred. Afterward, 1 g Ti₃AlC₂ powder was slowly added into the mixture in 5 min and stirred at 40 °C for 24 h. After etching process, the resultant mixture was washed via centrifugation (10 min at 3500 rpm) and the supernatant was decanted. Then a certain amount of DI water was added and the solution was hand-shaked for 5 min. The washing

process was repeated several times until the supernatant became dark-green and the pH is around 6. The supernatant was taken for next step.

Synthesis of Ca₂Nb_{3-x}Ta_xO₁₀ Nanosheets: The synthesis process is according to the literature.^[35] At first, bulk layered KCa₂Nb_{3-x}Ta_xO₁₀ was synthesized by combining K₂CO₃ (99.99%), CaCO₃ (99.99%), Nb₂O₅ (99.99%), Ta₂O₅ (99.99%) together by a molar ratio of K/Ca/Nb/Ta = 1.1:2:2.5:0.5. Then the mixture was ground for 30 min and then calcinated at 1100 °C for 10 h in air. The product was stirred in 3 M HNO₃ for 4 d and then washed several times before drying in the air. The white powder was then exfoliated via shaking for 7 d in 25% TBAOH solution. The fabrication of Ca₂Nb_{3-x}Ta_xO₁₀ nanosheets was completed by washing several times before use.

Device Fabrication: MXene/CNTO/CCI/Au: The Au pad as shown in the manuscript was fabricated by photolithography. Then 5 nm Cr and 30 nm Au were fabricated in turn through thermal evaporation. The bottom electrode was patterned through photolithography and MXene flakes are sprayed onto the substrate. Then the pattern of p-n junction was also fabricated by photolithography. N-type Ca₂Nb_{3-x}Ta_xO₁₀ nanosheets film was spin-coated two times after photolithography (1500 rpm, 30 s). P-type CsCu₂I₃ nanoparticle film was then fabricated through thermal evaporation after thoroughly grinding the mixture of CsI (99.999%) and CuI (99.95%) at the molar ratio of 1:2. The thickness of CsCu₂I₃ film was set as 100 nm. Then photolithography progress was applied again to pattern the Au top electrode, and it should be noted that during the photoresist removal process the acetone was replaced by 4-methyl-2-pentanone to avoid its influence on CsCu₂I₃ film.

MXene-LiF/CNTO/CCI/Au: The device fabrication procedure was almost the same as fabricating “MXene/CNTO/CCI/Au” device, only the sprayed MXene film was then coated with 5 nm LiF film through thermal evaporation.

MXene-Se/CNTO/CCI/Au: The device fabrication procedure was almost the same as fabricating “MXene-LiF/CNTO/CCI/Au” device, and the 5 nm LiF film was replaced by 5 nm Se film by thermal evaporation.

MXene-PEIE/CNTO/CCI/Au: The device fabrication procedure was almost the same as fabricating “MXene/CNTO/CCI/Au” device, only the MXene solution was replaced by the mixture of MXene and 0.4 wt% PEIE solution at the volume ratio of 1:1.

Au/CNTO/CCI/Au: The device fabrication procedure was almost the same as fabricating “MXene/CNTO/CCI/Au” device, except that sprayed MXene film was replaced by thermal evaporated Au film.

The active area of above devices are 300 μm × 300 μm (Figure 2d). The enlarged photograph of the device is attached in Figure S13 (Supporting Information).

Materials Characterization and Measurement of Photoresponse Performance: The morphology characterization was carried out by SEM (Zeiss Sigma). TEM, HRTEM, and SAED (JEM-1400 plus) were carried out for morphology and the crystal structure characterization. XRD patterns were obtained using Bruker D8 Advance X-ray diffractometer equipped with Cu Kα radiation (λ = 0.15406 nm). AFM and KPFM images were obtained using Bruker Dimension Icon. XPS spectra were obtained by using Thermo Scientific K-Alpha under the excitation of Al Kα (hν = 1486.6 eV). UV-vis spectra were obtained using a UV-vis spectrometer (Hitachi U-3900H). Raman was conducted by Dilor LabRam-1B via He-Ne laser of 4 mW with excitation wavelength of 532 nm. The optoelectronic properties were collected with the semiconductor characterization system (Keithley 4200-SCS) and a 70 W xenon arc lamp with a monochromator was used as light source. The light intensity was measured with a NOVA II power meter (OPHIR photonics). During image sensing tests, global array illumination was adopted and the probe was applied to collect photocurrents from only one pixel photodetector, ensuring there was no signal collected from other photodetectors. All the measurements were performed at room temperature.

Supporting Information

Supporting Information is available from the Wiley Online Library or from the author.

Acknowledgements

The work was supported by National Key R&D Program of China (No. 2018YFA0703700), National Natural Science Foundation of China (Nos. 12061131009 and 51872050), Science and Technology Commission of Shanghai Municipality (Nos. 21520712600 and 19520744300).

Conflict of Interest

The authors declare no conflict of interest.

Data Availability Statement

The data that support the findings of this study are available on request from the corresponding author. The data are not publicly available due to privacy or ethical restrictions.

Keywords

image sensing, logic electronics, MXenes, perovskites, photodetectors, tunable work function

Received: January 26, 2022

Revised: February 18, 2022

Published online:

- [1] Y. Liu, J. Guo, E. Zhu, L. Liao, S. J. Lee, M. Ding, I. Shakir, V. Gambin, Y. Huang, X. Duan, *Nature* **2018**, 557, 696.
- [2] J. Wang, J. Li, Y. Zhou, C. Yu, Y. Hua, Y. Yu, R. Li, X. Lin, R. Chen, H. Wu, H. Xia, H. L. Wang, *J. Am. Chem. Soc.* **2021**, 143, 7759.
- [3] F. Shahzad, A. Iqbal, H. Kim, C. M. Koo, *Adv. Mater.* **2020**, 32, 2002159.
- [4] J. L. Hart, K. Hantanasirisakul, A. C. Lang, B. Anasori, D. Pinto, Y. Pivak, J. T. van Omme, S. J. May, Y. Gogotsi, M. L. Taheri, *Nat. Commun.* **2019**, 10, 522.
- [5] A. VahidMohammadi, J. Rosen, Y. Gogotsi, *Science* **2021**, 372, 1165.
- [6] V. Kamysbayev, A. S. Filatov, H. Hu, X. Rui, F. Lagunas, D. Wang, R. F. Klie, D. V. Talapin, *Science* **2020**, 369, 979.
- [7] D. B. Velusamy, J. K. El-Demellawi, A. M. El-Zohry, A. Giugni, S. Lopatin, M. N. Hedhili, A. E. Mansour, E. D. Fabrizio, O. F. Mohammed, H. N. Alshareef, *Adv. Mater.* **2019**, 31, 1807658.
- [8] J. Zhou, X. H. Zha, M. Yildizhan, P. Eklund, J. Xue, M. Liao, P. O. A. Persson, S. Du, Q. Huang, *ACS Nano* **2019**, 13, 1195.
- [9] H. Xu, A. Ren, J. Wu, Z. Wang, *Adv. Funct. Mater.* **2020**, 30, 2000907.
- [10] S. Ahn, T. H. Han, K. Maleski, J. Song, Y. H. Kim, M. H. Park, H. Zhou, S. Yoo, Y. Gogotsi, T. W. Lee, *Adv. Mater.* **2020**, 32, 2000919.
- [11] H. Kim, M. I. Nugraha, X. Guan, Z. Wang, M. K. Hota, X. Xu, T. Wu, D. Baran, T. D. Anthopoulos, H. N. Alshareef, *ACS Nano* **2021**, 15, 5221.
- [12] K. Montazeri, M. Currie, L. Verger, P. Dianat, M. W. Barsoum, B. Nabet, *Adv. Mater.* **2019**, 31, 1903271.
- [13] J. Li, Z. Li, X. Liu, C. Li, Y. Zheng, K. W. K. Yeung, Z. Cui, Y. Liang, S. Zhu, W. Hu, Y. Qi, T. Zhang, X. Wang, S. Wu, *Nat. Commun.* **2021**, 12, 1224.
- [14] J. Xu, J. Shim, J.-H. Park, S. Lee, *Adv. Funct. Mater.* **2016**, 26, 5328.
- [15] W. Song, J. Chen, Z. Li, X. S. Fang, *Adv. Mater.* **2021**, 33, 2101059.
- [16] Z. Wang, H. Kim, H. N. Alshareef, *Adv. Mater.* **2018**, 30, 1706656.
- [17] Y. Liu, H. Xiao, W. A. Goddard3rd, *J. Am. Chem. Soc.* **2016**, 138, 15853.
- [18] A. Agresti, A. Pazniak, S. Pescetelli, A. Di Vito, D. Rossi, A. Pecchia, M. Auf der Maur, A. Liedl, R. Larciprete, D. V. Kuznetsov, D. Saranin, A. Di Carlo, *Nat. Mater.* **2019**, 18, 1228.
- [19] X. Xu, T. Guo, M. K. Hota, H. Kim, D. Zheng, C. Liu, M. N. Hedhili, R. S. Alsaadi, X. Zhang, H. N. Alshareef, *Adv. Mater.* **2021**, <https://doi.org/10.1002/adma.202107370>.
- [20] T. Schultz, N. C. Frey, K. Hantanasirisakul, S. Park, S. J. May, V. B. Shenoy, Y. Gogotsi, N. Koch, *Chem. Mater.* **2019**, 31, 6590.
- [21] A. Di Vito, A. Pecchia, M. Auf der Maur, A. Di Carlo, *Adv. Funct. Mater.* **2020**, 30, 1909028.
- [22] L. Yin, Y. Li, X. Yao, Y. Wang, L. Jia, Q. Liu, J. Li, Y. Li, D. He, *Nano-Micro Lett.* **2021**, 13, 78.
- [23] H. Jing, H. Yeo, B. Lyu, J. Ryou, S. Choi, J. H. Park, B. H. Lee, Y. H. Kim, S. Lee, *ACS Nano* **2021**, 15, 1388.
- [24] B. Lyu, M. Kim, H. Jing, J. Kang, C. Qian, S. Lee, J. H. Cho, *ACS Nano* **2019**, 13, 11392.
- [25] Y. Guo, T. Wang, Q. Yang, X. Li, H. Li, Y. Wang, T. Jiao, Z. Huang, B. Dong, W. Zhang, J. Fan, C. Zhi, *ACS Nano* **2020**, 14, 9089.
- [26] H. Wang, Y. Wang, Z. Ni, N. Turetta, S. M. Gali, H. Peng, Y. Yao, Y. Chen, I. Janica, D. Beljonne, W. Hu, A. Ciesielski, P. Samori, *Adv. Mater.* **2021**, 33, 2008215.
- [27] T. Aytun, A. Turak, I. Baikie, G. Halek, C. W. Ow-Yang, *Nano Lett.* **2012**, 12, 39.
- [28] Y. Zhou, C. Fuentes-Hernandez, J. Shim, J. Meyer, A. J. Giordano, H. Li, P. Winget, T. P. H. Cheun, J. Kim, M. Fenoll, A. Dindar, W. Haske, E. Najafabadi, T. M. Khan, H. Sojoudi, S. Barlow, S. Graham, J.-L. Brédas, S. R. Marder, A. Kahn, B. Kippelen, *Science* **2012**, 336, 327.
- [29] S. Xiong, L. Hu, L. Hu, L. Sun, F. Qin, X. Liu, M. Fahlman, Y. Zhou, *Adv. Mater.* **2019**, 31, 1806616.
- [30] A. Ren, J. Zou, H. Lai, Y. Huang, L. Yuan, H. Xu, K. Shen, H. Wang, S. Wei, Y. Wang, X. Hao, J. Zhang, D. Zhao, J. Wu, Z. Wang, *Mater. Horiz.* **2020**, 7, 1901.
- [31] T. Zhao, C. Zhao, W. Xu, Y. Liu, H. Gao, I. Z. Mitrovic, E. G. Lim, L. Yang, C. Z. Zhao, *Adv. Funct. Mater.* **2021**, 31, 2106000.
- [32] A. Sarycheva, Y. Gogotsi, *Chem. Mater.* **2020**, 32, 3480.
- [33] R. Li, X. Ma, J. Li, J. Cao, H. Gao, T. Li, X. Zhang, L. Wang, Q. Zhang, G. Wang, C. Hou, Y. Li, T. Palacios, Y. Lin, H. Wang, X. Ling, *Nat. Commun.* **2021**, 12, 1587.
- [34] G. Seo, H. Jung, T. D. Creason, V. Yeddu, M. Bamidele, E. Echeverria, J. Lee, D. McIlroy, B. Saparov, D. Y. Kim, *ACS Energy Lett.* **2021**, 6, 2584.
- [35] X. Liu, S. Li, Z. Li, Y. Zhang, W. Yang, Z. Li, H. Liu, D. V. Shtansky, X. S. Fang, *Adv. Funct. Mater.* **2021**, 31, 2101480.
- [36] X. Zhou, L. Zhang, Y. Huang, Z. Zhou, W. Xing, J. Zhang, F. Zhou, D. Zhang, F. Zhao, *Adv. Opt. Mater.* **2021**, 9, 2100889.
- [37] X. Li, L. Zhang, Q. Zheng, Z. Zhou, S. He, D. Tian, A. Guo, C. Wang, S. Liu, X. Chu, C. Yang, F. Zhao, *ACS Appl. Nano Mater.* **2022**, 5, 917.
- [38] Y. Zhang, S. Li, Z. Li, H. Liu, X. Liu, J. Chen, X. S. Fang, *Nano Lett.* **2021**, 21, 382.
- [39] F. P. García de Arquer, A. Armin, P. Meredith, E. H. Sargent, *Nat. Rev. Mater.* **2017**, 2, 16100.
- [40] Y. H. Chen, L. X. Su, M. M. Jiang, X. S. Fang, *J. Mater. Sci. Technol.* **2022**, 105, 259.
- [41] Z. Q. Li, Z. L. Li, Z. F. Shi, X. S. Fang, *Adv. Funct. Mater.* **2020**, 30, 2002634.
- [42] C. Zhu, X. Sun, H. Liu, B. Zheng, X. Wang, Y. Liu, M. Zubair, X. Wang, X. Zhu, D. Li, A. Pan, *ACS Nano* **2019**, 13, 7216.
- [43] W. Ouyang, J. X. Chen, Z. F. Shi, X. S. Fang, *Appl. Phys. Rev.* **2021**, 8, 031315.
- [44] Y. Liu, S. Wang, H. Liu, L. M. Peng, *Nat. Commun.* **2017**, 8, 15649.
- [45] J. Chen, Z. Li, F. Ni, W. Ouyang, X. S. Fang, *Mater. Horiz.* **2020**, 7, 1828.